



TECHNISCHE UNIVERSITÄT BERLIN

Zentrum für Astronomie und Astrophysik

**Bachelorthesis**

For acquisition of the degree

Bachelor of Science

**Parameter study of the evolution of a potential basal magma  
ocean on Mars**

supervised by

Dr. Sebastiano Padovan

Deutsches Zentrum für Luft- und Raumfahrt Berlin

submitted to

Prof. Dr. Dieter Breitschwerdt

Zentrum für Astronomie und Astrophysik

on September 21, 2020

by:

Illes Lohay

Mollwitzstraße 3

14059 Berlin

Tel. +4917658026153

E-Mail: logil1997@gmail.com

Course of studies: Physics, 9. Semester

Matriculation number: 169003692112

I hereby declare that the thesis is my own, unaided work, completed without any unpermitted external help. Only the sources and resources listed were used.

The independent and unaided completion of the thesis is affirmed by affidavit:

Berlin, September 21, 2020

A handwritten signature in black ink, appearing to read 'Korai'.

## Short Summary

The size of the core of Mars is currently not well constrained, with inferences based on the analysis of Martian meteorites pointing to a small core ( $\sim 1400$  km), while inferences based on the tidal response of the planet pointing to a larger core ( $\sim 1850$  km). These two estimates can be reconciled if at present a large basal magma ocean separates the core from the solid mantle. We develop a one-dimensional parameterized model of the interior of Mars to track the thermal evolution of the planet's interior and the fate of a putative basal magma ocean. While based on simplified physics, the simulations indicate that a basal magma ocean could be present on Mars today, thus providing a way to reconcile the different estimates of the size of its core.

## Kurze Zusammenfassung

Die Größe des Kerns vom Mars ist nach dem heutigen Wissensstand nicht präzise bestimmt. Es existieren die Werte, die sich auf der Analyse von Marsmeteoriten basieren ( $\sim 1400$  km), wobei die Gezeitenwechselwirkungen des Planeten auf einen größeren Kern hinweisen ( $\sim 1850$  km). Diese beide Modelle können miteinander vereinbart werden, wenn derzeit ein großes Basal Magma-Ozean den Kern und den Mantel separiert. Wir entwickeln eindimensionale parametrisierte Modelle der inneren Aufbau vom Mars um die thermische Evolution des Planeteninneren zu verfolgen sowie auch das Schicksal vom Basal Magma-Ozean zu bestimmen. Die auf der vereinfachten Physik basierende Simulationen weisen auf die mögliche Existenz eines derzeitigen Magma-Ozeans auf dem Mars, was beide Theorien miteinander vereinbart.

# Contents

<b>1</b>	<b>Introduction</b>	<b>1</b>
<b>2</b>	<b>Theory</b>	<b>3</b>
2.1	Four-Layer Mars Model . . . . .	3
2.2	Heat production . . . . .	5
2.3	Parameterized Thermal Evolution Model . . . . .	8
2.3.1	Energy balance equations . . . . .	8
2.3.2	Stagnant lid thickness . . . . .	10
2.3.3	Heat fluxes . . . . .	11
2.4	Melting curves . . . . .	12
2.5	Surface temperature $T_{surf}$ . . . . .	13
2.6	Temperature adjustment . . . . .	14
<b>3</b>	<b>Results and discussion</b>	<b>15</b>
3.1	Approach . . . . .	15
3.2	Parameters range . . . . .	15
3.3	Global input parameter variations . . . . .	16
3.4	Influence of input parameter variations on one model . . . . .	19
3.5	Magmatic activity . . . . .	22
<b>4</b>	<b>Conclusions</b>	<b>23</b>
<b>5</b>	<b>References</b>	<b>24</b>
<b>6</b>	<b>Appendix</b>	<b>A1</b>

# 1 Introduction

The current understanding of the terrestrial planet formation suggests an early phase where the majority of the body is in a molten state [Elkins-Tanton, 2012]. The heat required to melt the interior of the planet is expected to be generated by the three main mechanisms: kinetic energy transfer during the accretion of the planetesimals, the metal-silicate differentiation—which leads to the core-mantle separation—and, depending on the timing of formation, the decay of the short-lived radiogenic elements (e.g.  $^{26}\text{Al}$ , with the half-life time of 0.74 Ma.). During this primordial magma ocean phase, the heat stored in the interior is removed through the planetary surface by convective heat transfer in the magma ocean.

The cooling of this primordial magma ocean is marked with its bottom-up solidification, with iron and radionuclides preferentially remaining within the liquid phase, leading to a scenario where enriched liquid magma ocean overlays a depleted mantle [Elkins-Tanton, 2012]. Once the primordial magma ocean is fully solidified, the interior structure is gravitationally unstable, likely leading to a global mantle overturn, where the dense material sinks to the core-mantle-boundary(CMB), while lighter material drifts to the top, thus forming a stable chemically-layered interior [Plesa et al., 2014].

After the global overturn, the radiogenic elements that are displaced with the iron-rich cumulates to the CMB, increase the bottom mantle temperature [Plesa et al., 2014]. Under reasonable overturn scenarios, the high abundance of heat producing elements in the bottom part of the mantle is compatible with its liquefaction, in other words with the creation of a basal magma ocean [Plesa et al., 2014].

The core of Mars is commonly expected to be metallic, while also containing light-alloying elements, most likely in the form of sulfur. The amount of sulfur in the core correlates with its size, since given the total mass of the planet, the denser the core—i.e., the less sulfur it contains—the smaller its size. The size of the core of Mars can be estimated both with geodetical and geochemical methods. Geodetical methods are based on estimates of the tidal response of Mars, which is very sensitive to the radius of the largest global liquid layer in the interior, in this case the core [Yoder et al., 2003]. This approach favours a core radius larger than about 1800 km [Plesa et al., 2018]. If sulfur is the only light-alloying element in the core, such large cores would correspond to a core sulfur content in excess of about 14 wt% [Rivoldini et al., 2011]. Geochemical methods based on the analysis of martian meteorites indicates a core sulfur content  $<5$  wt% [Wang and Becker, 2017], which would correspond to a core radius  $< 1500$  km [Rivoldini et al., 2011]. The presence of a BMO provides a mean to reconcile these two estimates, since being liquid it would count as core material in the geodetical methods, while being made of liquefied mantle material, its volume does not count as

## *1 Introduction*

core from the geochemical point of view.

In this thesis, we develop one-dimensional parameterized models to track the thermal evolution of the interior of Mars and the fate of a putative BMO.

## 2 Theory

The proper investigation of the evolution of the magma ocean requires the knowledge of the planet's interior structure and a model for its thermal evolution.

### 2.1 Four-Layer Mars Model

The interior structure of Mars can be firstly approximated with a two-layer model, consisting of a dense spherically symmetric and homogeneous core surrounded by a homogeneous silicate shell. The mean density  $\bar{\rho}$  of this model planet can be derived as:

$$\bar{\rho}R_p^3 = \rho_c r_c^3 + \rho_b(R_p^3 - r_c^3), \quad (1)$$

where  $\rho_c$  and  $\rho_b$  are the core and silicate bulk densities, respectively,  $R_p$  is the volumetric mean radius of Mars and  $r_c$  is the radius of the core. Similarly, the moment of inertia (MOI) is:

$$MOI = nM_p R_p^2 = \frac{8\pi}{15} r_c^5 \rho_c + \frac{8\pi}{15} (R_p^5 - r_c^5) \rho_b \quad (2)$$

where  $n$  is the moment of inertia factor, a parameter proportional to the central concentration of matter in the subsurface whose theoretical limits are 0.4 for a homogeneous sphere and 0 for a point mass. Indicating with  $\alpha = \frac{r_c}{R_p}$  the ratio between the radius of the core and that of the planet, the previous two equations can be thought of as a system with three unknowns:  $\rho_b$ ,  $\rho_c$  and  $\alpha$ . In this work we will vary the value of the radius of the core and accordingly, obtain the core and silicate densities.

The silicate bulk is further divided into three layers. From the surface inward:

1. Crust with thickness  $h$  and density  $\rho_{cr}$ ;
2. Depleted mantle of density  $\rho_b$  ;
3. Magma ocean of thickness  $t$  and density  $\rho_{MO}$ .

The mass balance applied to the three components of the bulk silicate layer reads:

$$\rho_b(R_p^3 - r_c^3) = \rho_{MO} [(r_c + t)^3 - r_c^3] + \rho_m [(R_p - h)^3 - (r_c + t)^3] + \rho_{cr} [R_p^3 - (R_p - h)^3], \quad (3)$$

where we further assume that the density of the depleted mantle  $\rho_m$  equals the density of the silicate bulk  $\rho_b$  obtained from Eq.(1) and (2).

The density of magma ocean  $\rho_{MO}$  from Eq. (3) is:

$$\rho_{MO} = \frac{\rho_b [(r_c + t)^3 - r_c^3] + \rho_{cr} [R_p^3 - (R_p - h)^3]}{(r_c + t)^3 - r_c^3} = \rho_b + (\rho_b - \Delta\rho) \frac{[R_p^3 - (R_p - h)^3]}{(r_c + t)^3 - r_c^3}, \quad (4)$$

## 2 Theory

where we set a constant density contrast between the mantle and the crust  $\Delta\rho$ . Values for the crustal thickness  $h$  can be obtained from analyses of gravity and altimetry data [e.g., Goossens et al., 2017]. Finally, by setting the thickness of the magma ocean  $t$  provides the magma ocean density  $\rho_{MO}$ .

Using Eq.(1) and (2), we estimate pairs of mantle and core densities. They depend on the core-planetary radius ratio  $\alpha = \frac{R_c}{R_p}$ , moment of inertia factor  $n$  and mean density of the planet  $\bar{\rho}$ . Fig. 1 illustrates how these variables depend on each other. Using both geochemical and geodetical estimates for the core radius [Rivoldini et al., 2011; Wang and Becker, 2017; Plesa et al., 2018], we investigate the range  $R_c = [1400, 1800]$  km, which corresponds to a variation of the  $R_c/R_p$  ratio in the range  $[0.41, 0.53]$ . These two values are plotted as red dots in Figure 1. We expect the silicate bulk density of Mars to be of a factor 0.9 of the mean density of the planet, while the core density can significantly vary in the range  $[1.6\bar{\rho}, 2.4\bar{\rho}]$ . Having estimated both core and bulk silicate densities, we can extend the two-layer-model to the four-layer-model.

Eq. (4) is used to calculate the density variations of the magma ocean  $\rho_{MO}$  as a function of its

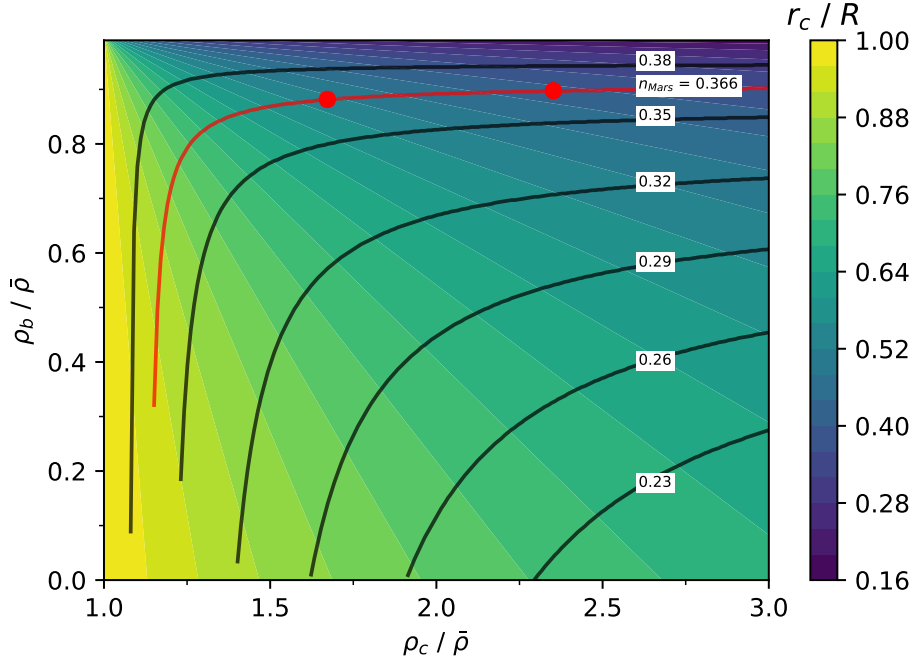


Figure 1: Two-layer-model of the interior and the corresponding core and mantle densities. Background color-coded according to the core to planetary radius ratio  $\alpha$ . Black curves represent models with constant normalized moment of inertia  $n$ , indicated in the label. The red curve corresponds to the value of Mars  $n = 0.366$  NASA [2020].



## 2 Theory

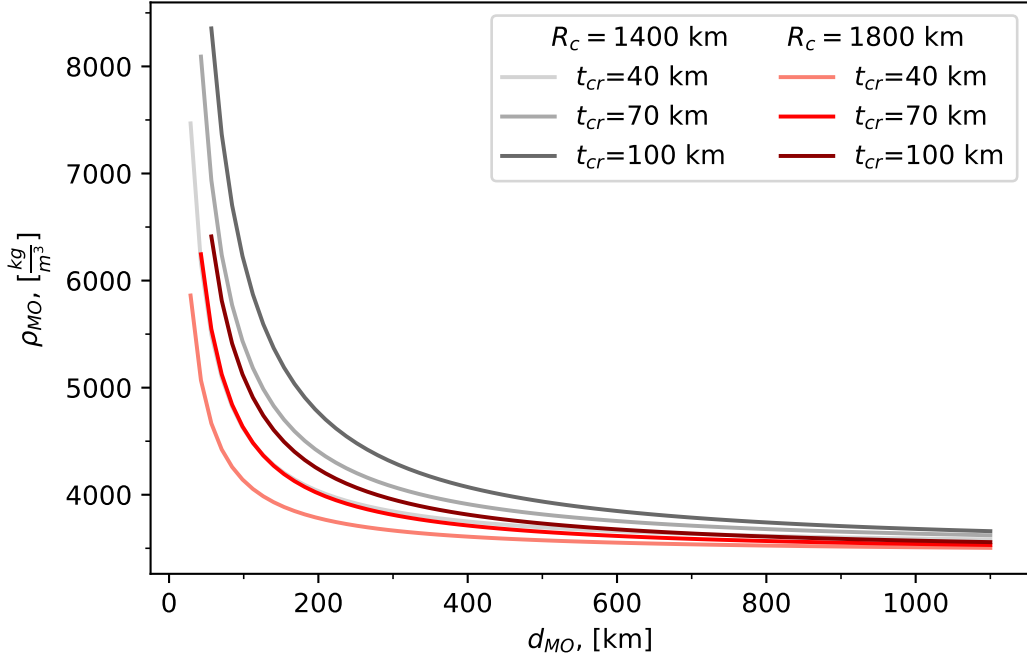


Figure 2: Four-layer-model with density of the magma ocean  $\rho_{MO}$  as a function of its thickness  $t$  for two different values of the radius of the core.

thickness  $t$ . We vary the core size  $r_c$ , the thickness of the crust  $t_{cr}$ , while using a value for the mantle-crust density contrast from Neumann et al. [2004] to arrive the dependencies shown in Fig. 2.

The density of the magma ocean steadily decreases for increasing  $d_{MO}$ , down to the value of  $\rho_{MO} \approx 3500 \frac{\text{kg}}{\text{m}^3}$  for  $d_{MO} = 600$  km, thenceforth remaining constant and almost independent of the core radius  $r_c$ . In Fig. 2, each curve is cut at a maximum density to ensure that the structure is gravitationally stable, i.e., that the density of the MO,  $\rho_{MO}$ , is lower than the density of the core  $\rho_c$ .

### 2.2 Heat production

The main source of heat within the planet is the internal heat generated by the decay of the radioactive elements. The relevant radionuclides are  $^{40}\text{K}$ ,  $^{232}\text{Th}$ ,  $^{235}\text{U}$  and  $^{238}\text{U}$ . The heat production rate per unit mass  $H_{mass}$  after a time  $t$  from the begin of the decay can be calculated via [e.g.,

## 2 Theory

Turcotte and Schubert, 2014]:

$$H_{mass} = \sum_{i=1}^4 A^i \cdot C_0^i H_0^i \exp\left(\frac{-t \ln 2}{\tau^i}\right), \quad (5)$$

where, for each element  $i$ ,  $A^i$  indicates its natural abundance,  $C_0^i$  the initial concentration,  $H_0^i$  the specific heat production rate measured in  $\frac{\text{W}}{\text{kg}}$ , and  $\tau^i$  the half-life. The values for  $H_0$ ,  $A$  and  $\tau$  are taken from Breuer [2009]. We assume the initial heat-source concentrations within the silicate bulk of the Mars as in the model of Wänke and Dreibus [1994]. All values are listed in Table 5 of the Appendix.

The enrichment factor  $\Lambda_i$  for each layer  $i$  is defined as the ratio of the heat production per unit mass between the layer  $i$  and the silicate bulk  $b$ :

$$\Lambda_i = \frac{H_i}{H_b}. \quad (6)$$

A mass balance equation for the heat sources in the silicate bulk reads:

$$M_b = \Lambda_{cr} M_{cr} + \Lambda_m M_m + \Lambda_{MO} M_{MO}. \quad (7)$$

The crustal enrichment is based on the surface composition. Despite the data for the surface composition are strictly valid only for the very few top centimetres of the crust, we make the usual assumption that the crust has a constant enrichment [e.g. Plesa et al., 2015]. Since both the crust and the magma ocean are enriched (Sec. 1), the mantle is depleted with respect to the initial silicate bulk ( $\Lambda_m < 1$ ).

We use Eq. (7) and the relation among the density and thickness of the various layers from Sec. 2.1 to estimate the enrichment factor of the magma ocean  $\Lambda_{MO}$  and its dependency on the other enrichment values. For that we apply a range of the depleted mantle enrichments  $\Lambda_m[0.1, 0.7]$  and crustal enrichments  $\Lambda_{cr}[9, 15]$ .

Taking the specific heat production rate  $H$ , abundance  $A$  and the half-life  $\tau$  of the isotopes introduced in 2.2 from Breuer [2009] and using the concentrations  $C$  from Wänke and Dreibus [1994], we can calculate the total heat production  $H_{mass}$  via Eq. (5). The exponential decrease with time of the total heat generated is shown on Fig. 3. The main heat sources in the early stage of evolution of Mars are therefore  $^{40}\text{K}$  and  $^{235}\text{U}$ , while at present heat is mostly generated by  $^{232}\text{Th}$  and  $^{238}\text{U}$ . The heat generated in the magma ocean is obtained from its enrichment factor  $\Lambda_{MO}$ , estimated from the Eq. (7). The variation of the enrichment factors of crust, mantle and magma ocean for two end member models ( $r_c = 1400$  km,  $t_{MO} = 500$  km and  $r_c = 1800$  km,  $t_{MO} = 100$  km) are shown in Figure 4. To make the comparison easier, we use the same colour scaling for both models.

## 2 Theory

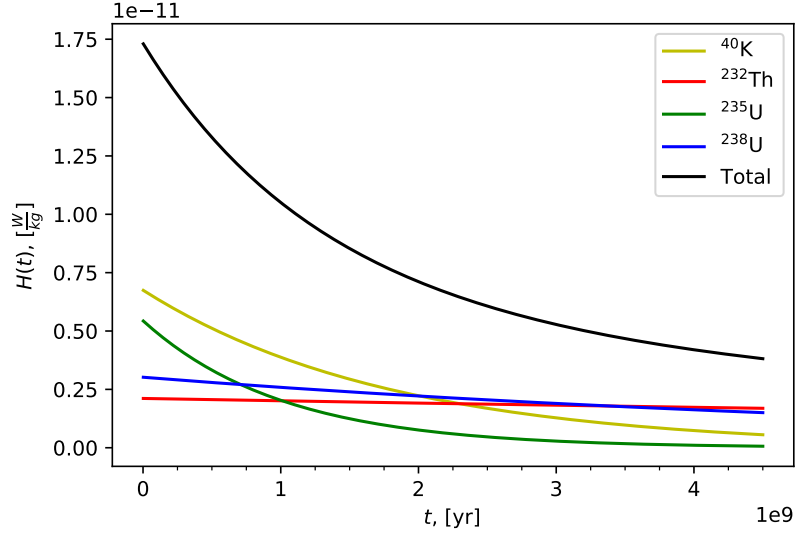


Figure 3: Elementwise and total generated heat within Mars interior. The shape of curves depends on the half-life of the elements, listed in the Appendix.

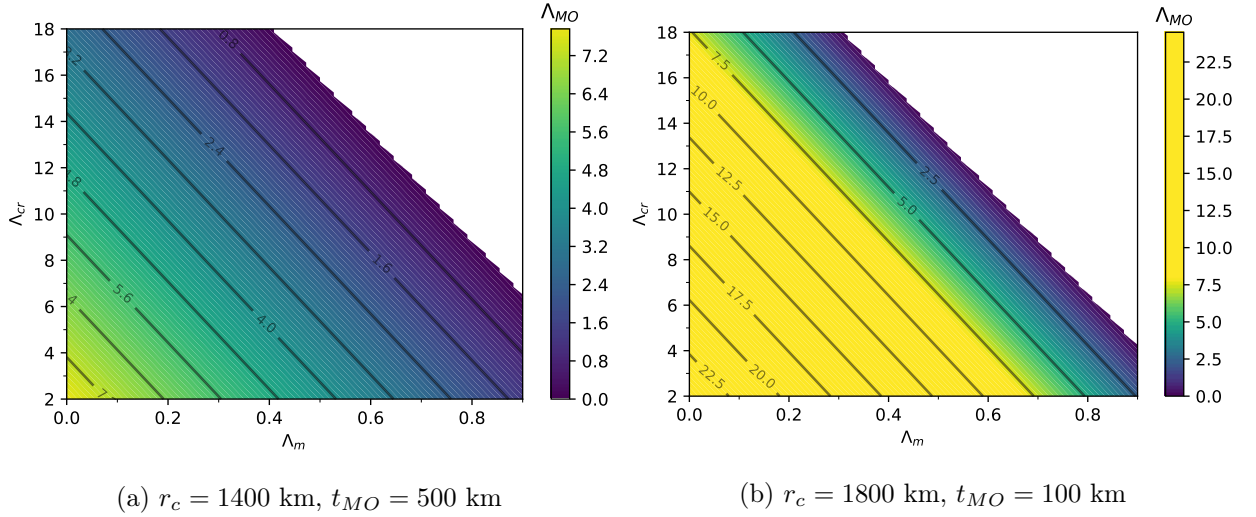


Figure 4: Two example models with the same magma ocean-mantle transition at 1900 km and crustal thickness of  $t_{cr} = 45$  km, though with a different core radii and magma ocean thicknesses, as shown in the labels. Only physically possible enrichment values of  $\Lambda_{MO}$  are plotted.

As expected, a low enrichment of the mantle and the crust corresponds to an extremely enriched magma ocean.

## 2.3 Parameterized Thermal Evolution Model

The thermal evolution of the planet is modelled by keeping track of how energy in the interior is removed from the planet through the surface. We adopt an approach that is a simplified version of Grott and Breuer [2008], but with an important modification that allows for the treatment of a basal magma ocean. The model is illustrated in Fig. 5, which shows the interior structure, melting curves (Sec. 2.4) and a representative temperature profile.

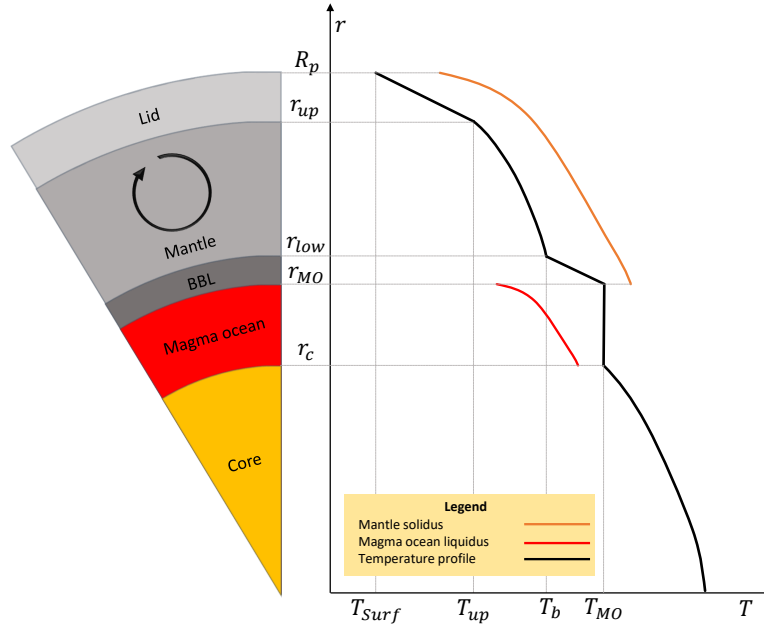


Figure 5: An illustration of the interior structure and the corresponding temperature profile. The isothermal magma ocean overlays the convective core. Energy transfer in the solid mantle occurs through the convective layer, which is located between the conductive stagnant lid and bottom boundary layer. Courtesy of Dr. S. Padovan.

### 2.3.1 Energy balance equations

The thermal state of the mantle can be described through the energy conservation equation, which, indicating with  $C_p$  the heat capacity,  $M = \rho V$  the mass,  $q_{low}$  and  $q_{up}$  the heat fluxes entering the convective mantle and the stagnant lid,  $A_i$  the corresponding surface area of the radius  $r_i$  and  $H$

## 2 Theory

the heat production per unit mass within the layer, reads:

$$C_{pm}\rho_m \frac{d}{dt} \left( \int_{V_m} T(r,t) dV_m \right) = q_{low}(t)A_{low}(t) - q_{up}(t)A_{up}(t) + M_m(t)H_m(t), \quad (8)$$

where the time variation of the energy content of the mantle on the left side is the result of the heat gained from the underlying liquid interior (magma ocean and core)  $q_{low}(t)A_{low}(t)$ , the heat leaving through the lid  $q_{up}(t)A_{up}(t)$  and the internal heat produced through the decay of the radionuclides  $M_m(t)H_m(t)$ .

If the volume of the mantle is constant, the integral on the left side of the equation (8) can be rewritten in the following manner:

$$\frac{d}{dt} \int_{V_m} T(r,t) dV_m = V_m \frac{d}{dt} \left( \frac{\int_{V_m} T(r,t) dV_m}{V_m} \right) = V_m \frac{d \langle T_m \rangle}{dt}, \quad (9)$$

which expresses the total time variation of the temperature within the finite volume of the mantle in terms of the mantle average temperature  $\langle T_m \rangle$ . Using the adiabatic mantle temperature profile  $T(r) = T_{up} \exp[\alpha g / C_{pm} (r_{up} - r)]$ , the average mantle temperature at the given point in time can be written as  $\langle T_m \rangle = \lambda_t T_{up}$ , where  $\lambda_t$  must be computed at each time step. Thus, Eq. (9) can be rewritten as:

$$C_{pm} M_m \lambda_t \frac{dT_{up}}{dt} = q_{low}(t)A_{low}(t) - q_{up}(t)A_{up}(t) + M_m H_m(t). \quad (10)$$

The combined time variation of the energy of the basal magma ocean and the core can be described as:

$$C_{pmo}\rho_{mo} \frac{d}{dt} \left( \int_{V_{mo}} T(r,t) dV_{mo} \right) + C_{pc}\rho_c \frac{d}{dt} \left( \int_{V_c} T(r,t) dV_c \right) = -q_{low}(t)A_{low}(t) + M_{mo}(t)H_{mo}(t) + \rho_{mo}L_{crist} \frac{dV_{mo}}{dt}, \quad (11)$$

where  $L_{crist}$  is the latent heat of solidification of the magma ocean. As for Eq. (8), the terms on the left hand side are the variations of the energy content of the core and the magma ocean as the result of the heat lost  $-q_{low}(t)A_{low}(t)$  to the convective mantle, heat gained through the decay of the radionuclides within the magma ocean  $M_{mo}(t)H_{mo}(t)$  and heat received through the solidification of the magma ocean  $\rho_{mo}L_{crist} \frac{dV_{mo}}{dt}$ . We also assume the absence of the radionuclides within the core of the planet.

We do not consider the growth of the inner core in this model. According to Grott and Breuer [2008], such growth would induce the chemical dynamo of Mars and generate long-time global magnetic field, thus conflicting with the expected brief early Mars dynamo [e.g., Williams and

## 2 Theory

Nimmo, 2004]. Therefore, the core radius is constant and the core heat variations can be treated analogously to the heat variations of the convective mantle within Eq. (9). Additional assumptions of the adiabatic core temperature profile, constant temperature of the magma ocean, core density and heat capacity leads to:

$$C_{pc}\rho_c \frac{d}{dt} \left( \int_{V_c} T(r, t) dV_c \right) = \lambda_{c1} C_{pMO} \lambda_{c2} \rho_{MO} \lambda_{c3} V_c \frac{dT_{MO}}{dt} = \lambda_{ct} C_{pMO} \rho_{MO} V_c \frac{dT_{MO}}{dt} \quad (12)$$

where the  $\lambda_{ct} = \lambda_{c1} \lambda_{c2} \lambda_{c3} = \frac{C_{pc}}{C_{pMO}} \cdot \frac{\rho_c}{\rho_{MO}} \cdot \frac{V_c}{V_{MO}}$  needs to be calculated at each time point  $t$ , similarly to the  $\lambda_t$  in Eq. (10).

The thickness of the magma ocean may vary over time if crystallization occurs, thus the first integral of equation (11) will have time-dependent boundary  $r_{MO}(t)$ , while the core radius is constant. Such an integral can be calculated using the Leibniz's integral rule:

$$\frac{d}{dt} \int_{r_c}^{r_{MO}} T(r, t) 4\pi r^2 dr = 4\pi T(r_{MO}, t) r_{MO}^2 \frac{dr_{MO}}{dt} - 4\pi T(r_c, t) r_c^2 \frac{dr_c}{dt} + 4\pi \int_{r_c}^{r_{MO}} \frac{dT(r, t)}{dt} r^2 dr \quad (13)$$

The length scale of the adiabatic temperature profile within the magma ocean is  $\sim 12000$  km, therefore we make the assumption that  $T_{MO}(r, t) = T_{MO}(t)$ . With the magma ocean temperature being independent of depth, the first term can be rewritten as  $4\pi T_{MO} \frac{dV_{MO}}{dt}$ . This term describes the heat loss associated with the volume changes of the magma ocean, which would require an analogous term on the right side of the Eq. (11) to account the energy contribution from the variation of volume of the magma ocean, thus cancelling itself out. The second term on the right side of the Eq. (13) is zero due to the fixed core radius. The third term describes the energy change through the temperature variations across the magma ocean with fixed borders, analogous to the term within the Eq. (9).

Assuming the absence of the heat-producing-elements within the core and taking into account the possible partial solidification of the magma ocean, the energy balance equation for magma ocean and core is given by:

$$C_{pMO} \rho_{MO} [V_{MO} + \lambda_{ct} V_c] \frac{dT_{MO}}{dt} = -q_{low}(t) A_{low}(t) + M_{MO}(t) H_{MO}(t) + \rho_{MO} L_{crist} \frac{dV_{MO}}{dt} \quad (14)$$

### 2.3.2 Stagnant lid thickness

The thickness of the stagnant lid  $d_{lid}$  is calculated by rearranging the Fourier equation of the heat conduction in the following way:

$$d_{lid} = k_m \frac{T_{up} - T_{surf}}{q_{up}} \quad (15)$$

## 2 Theory

where  $k_m$ ,  $T_{up}$ ,  $T_{surf}$ ,  $q_{up}$  are the mantle thermal conductivity, upper mantle temperature, surface temperature and heat flux leaving the convective mantle (Fig. 5).

Since the stagnant lid is positioned between the mantle and the surface, it completely includes the crust, which is highly enriched with the radionuclides and the depleted mantle. The lid enrichment factor  $\Lambda_{lid}$  is calculated using the following mass balance equation for the heat-producing-elements:

$$\Lambda_{lid}(R_p^3 - r_{up}^3) = \Lambda_{cr}[R_p^3 - (R_p - d_{cr})^3] + \Lambda_m[(R_p - d_{cr})^3 - r_{up}^3] \quad (16)$$

For simplicity, we neglect here the density contrast  $\Delta\rho$  between the crust and the mantle, while only taking into account the enrichment factor of each layer.

### 2.3.3 Heat fluxes

The upper boundary heat flux  $q_{up}$  is defined through a parameterization based on Reese et al. [1998]:

$$q_{up} = \frac{1}{2}k_m \frac{T_{up}(t) - T_{surf}}{D_m} \cdot \gamma^{-4/3} Ra^{1/3} \quad (17)$$

where  $k_m$  and  $D_m$  are the thermal conductivity and thickness of the convective mantle.  $T_{up}$  and  $T_{surf}$  are the temperature at the stagnant lid - convective mantle boundary and at the surface.  $\gamma$  is a dimensionless parameter and  $Ra$  is the Rayleigh number, which are defined as:

$$\gamma = \frac{E^*[T_{up}(t) - T_{surf}]}{RT_{up}(t)^2}, \quad (18)$$

$$Ra = \frac{\rho_m g \alpha_m (T_{up}(t) - T_{surf}) D_m^3}{\eta[T_{up}(t)] \kappa_m}, \quad (19)$$

where  $E^*$ ,  $R$ ,  $\rho_m$  and  $g$  are the activation energy, universal gas constant, mantle density and the surface gravitational acceleration of Mars. The parameters  $\alpha_m$  and  $\kappa_m$  are the mantle thermal expansivity and thermal diffusivity. The temperature-dependent viscosity  $\eta$  is assumed to obey an Arrhenius law, which is given by:

$$\eta[T] = \eta_{ref} \exp\left[\frac{E^*}{R}\left(\frac{1}{T} - \frac{1}{T_{ref}}\right)\right], \quad (20)$$

with the reference viscosity  $\eta_{ref}$  corresponding to the reference temperature  $T_{ref}$ .

The flux flowing through the bottom boundary layer is given by the Fourier law applied to the boundary layer of thickness  $\delta_{low}$  with the temperature difference of  $T_{MO} - T_b$ , resulting in:

$$q_{low} = k_m \frac{T_{MO} - T_b}{\delta_{low}}, \quad (21)$$

## 2 Theory

	Value	Unit		Value	Unit
$A_1$	1340.38	K	$B_1$	975	K
$A_2$	130.33	K · GPa <sup>-1</sup>	$B_2$	62.5	K · GPa <sup>-1</sup>
$A_3$	- 6.37695	K · GPa <sup>-2</sup>			
$A_4$	0.118912	K · GPa <sup>-3</sup>			

Table 1: Parameters obtained from Ruedas and Breuer [2017] and used to calculate the solidus temperature.

where  $T_b$  is the temperature of the bottom of the convective mantle, defined through its adiabatic temperature profile. For the thickness of the bottom boundary layer we use the equation proposed by Stevenson et al. [1983]:

$$\delta_{low} = (R_p - r_{low}) \left[ \frac{Ra_{crit}}{Ra_{loc}} \right]^\beta. \quad (22)$$

$Ra_{crit}$  is the critical Rayleigh number, above which the layer destabilizes. We take  $Ra_{crit} = 450$  and  $\beta = 0.3$  [Stevenson et al., 1983].  $Ra_{loc}$  is the Rayleigh number evaluated locally and given by [Stevenson et al., 1983]:

$$Ra_{loc} = \frac{\rho_m g \alpha_m [T_{up} - T_{surf} - (T_{MO} - T_b)] D_m^3}{\eta[T_b] \kappa_m} \quad (23)$$

### 2.4 Melting curves

The solidus curve describes, as a function of depth (equivalently, pressure), the temperature above which rocks would start melting. The liquidus curves describes the temperature, above which the material would be completely molten. These two curves are referred to as “melting curves”. For the solidus temperature of Mars, we adopt the parameterization of Ruedas and Breuer [2017] in terms of pressure  $p$  :

$$T_{sol} \begin{cases} A_1 + A_2 p + A_3 p^2 + A_4 p^3 & , p \leq 23 \text{ GPa} \\ B_1 + B_2 p & , \text{otherwise} \end{cases} \quad (24)$$

where the coefficients  $A_i$  and  $B_i$  are listed in Table 1 and  $p$  is given in GPa. The pressure increase within the planetary interior can be calculated with the equation of hydrostatic equilibrium [e.g., Turcotte and Schubert, 2014]:

$$\frac{dp}{dr} = -\rho(r)g(r), \quad (25)$$



## 2 Theory

with  $\rho$  the density and  $g$  the gravitational acceleration, which for a spherically symmetric body is given by:

$$g(r) = \frac{GM(r)}{r^2}, \quad (26)$$

where  $M(r)$  is the mass of material located below radius  $r$ . For the two-layer model consisting of core and silicate bulk with constant densities  $\rho_c$  and  $\rho_b$ , respectively, the gravitational acceleration is:

$$g(r) = \begin{cases} \frac{4\pi G}{3} r \rho_c & 0 \leq r \leq R_c, \\ \frac{4\pi G}{3} (r \rho_b + \frac{R_c^3}{r^2} (\rho_c - \rho_b)) & R_c \leq r \leq R_p. \end{cases} \quad (27)$$

Inserting Eq. (27) into Eq. (25) and integrating it over the radius  $r$ , we obtain the expression for the pressure  $p$ :

$$p(r) = \begin{cases} \frac{2\pi G \rho_c^2}{3} (R_c^2 - r^2) + \frac{2\pi G \rho_b^2}{3} (R_p^2 - R_c^2) + \frac{4\pi G \rho_b R_c^3}{3} (\rho_c - \rho_b) \left( \frac{1}{R_c} - \frac{1}{R_p} \right) & , 0 \leq r \leq R_c \\ \frac{2\pi G \rho_b^2}{3} (R_p^2 - r^2) + \frac{4\pi G \rho_b R_c^3}{3} (\rho_c - \rho_b) \left( \frac{1}{r} - \frac{1}{R_p} \right) & , R_c \leq r \leq R_p \end{cases} \quad (28)$$

Inserting Eq. (28) into Eq. (24) provides the solidus curve for the mantle.

We investigate scenarios where the solid mantle overlays the liquid magma ocean. For this to be possible, the temperature at the magma ocean-mantle transition shall be higher then the magma ocean liquidus, but lower then the mantle solidus.

We define the liquidus in the magma ocean as a temperature-shifted mantle solidus with a dependency on the magma ocean  $\Lambda_{MO}$ , since higher HPE content corresponds to a lower liquidus:

$$T_{liq} = T_{sol} - \Delta T = T_{sol} - 100 \cdot \ln(\Lambda_{MO} - \Lambda_m) - \Delta T_0 \quad (29)$$

where  $\Delta T_0 = 500$  K is the initial temperature shift at the beginning of the evolution and a factor of 100 is used to ensure that the temperature shift severely increases for the higher magma ocean enrichment. This approach is empirical and avoids the details of the effect of the solidification on the magma ocean enrichment and relative liquidus variation, which have effects similar to variation of other model parameters (see the next Section).

### 2.5 Surface temperature $T_{surf}$

The surface temperature can be derived from an energy balance at the planetary surface. The heat emitted through the entirety of the surface is the result of the solar radiation and of the inner heat

## 2 Theory

flow  $q_s$ , according to:

$$\frac{4\pi R_s^2 \sigma T_s^4}{4\pi d^2} \cdot \pi R_p^2 (1 - A) + q_s 4\pi R_p^2 = 4\pi R_p^2 \sigma T_{surf}^4 \quad (30)$$

where  $R_s$  and  $T_s$  are the radius and effective temperature of the Sun,  $d$  is the semimajor axis of Mars and  $A$  the geometric albedo of the planet. Based on estimates of the inner heat flow from Plesa et al. [2016] the second term on the left hand side of Eq. (30) is negligible. The surface temperature can therefore be estimated as:

$$T_{surf} = T_s \left( \frac{R_s}{2d} \right)^{\frac{1}{2}} \cdot (1 - A)^{\frac{1}{4}} \quad (31)$$

### 2.6 Temperature adjustment

The parameterized thermal evolution model described in Sec. 2.3 consists of two equations: Eq. (10) describing the energy conservation within the mantle and Eq. (14) characterizing the core and magma ocean reservoirs. Both include the time derivative of the temperature, which can be discretized as  $\frac{dT}{dt} = \frac{T^{n+1} - T^n}{\Delta t}$ , making it possible to determine the new temperature  $T^{n+1}$  after time  $\Delta t$  passed if the initial temperature  $T^n$  is given. Thus, we discretize the two energy conservation equations as:

$$T_{up}^{n+1} = T_{up}^n + \frac{\Delta t}{M_m C_{p_m} \lambda_t} (q_{low} A_{low} - q_{up} A_{up} + M_m H_m) \quad (32)$$

$$T_{MO}^{n+1} = T_{MO}^n + \frac{\Delta t}{\rho_{MO} C_{p_{MO}} [V_{MO} + \lambda_{c_t} V_c]} \left( -q_{low} A_{low} + M_{MO} H_{MO} + L_{crist} \left[ \rho_{MO} \frac{dV_{MO}}{dt} - \rho_m \frac{dV_m}{dt} \right] \right) \quad (33)$$

### 3 Results and discussion

#### 3.1 Approach

The thermal evolution of Mars is modelled with the parameterized model described in the previous sections and implemented as a python code. The code implements the four-layer-model of Mars, introduced in Sec. 2.1, determines the enrichment factor  $\Lambda_{MO}$  and the density  $\rho_{MO}$  of the basal magma ocean with the approach discussed in Sec. 2.2 and calculates the solidus curve to estimate the initial possible temperature of the MO,  $T_{MO}$ . Using the established temperature profile, the code calculates possible crystallization volume of the magma ocean, followed by solving the energy balance equations (10) and (14) to determine the new upper mantle temperature  $T_{up}$  and the temperature of the BMO,  $T_{MO}$ . Simultaneously, the stagnant lid thickness  $d_{lid}$ , the thickness of the bottom-boundary-layer  $d_{bbl}$ , the upper and lower mantle heat fluxes  $q_{up}$  and  $q_{low}$  are calculated. The code tracks the changes of these parameters for the whole span of the 4.5 billion years every timestep  $\Delta t = 4 \cdot 10^6$  y. The initial conditions of the thermal model correspond to a set of eight parameters, listed in Table 2.

#### 3.2 Parameters range

We use core radii in the range [1300, 1500] km, which are consistent with recent studies [Rivoldini et al., 2011; Wang and Becker, 2017; Plesa et al., 2018], while also applying a range ([400, 600] km) of possible initial thicknesses of the MO. The initial temperature of the MO,  $T_{MO}$ , is limited by the mantle solidus curve and the BMO liquidus curve, thus variations in the range [1900, 2100] K are considered. We also test the influence of the different initial upper mantle temperatures

Parameter	Description	Value ranges
$r_c$	Core radius	[1300, 1500] km
$d_{MO}$	MO thickness	[400, 600] km
$T_{MO}$	MO initial temperature	[1900, 2100] K
$T_{up}$	Upper mantle temperature	[1600, 1900] K
$\lambda_{cr}$	Enrichment factor of the crust	[9, 15]
$\lambda_m$	Enrichment factor of the mantle	[0.1, 0.7]
$\eta_{ref}$	Reference viscosity	$[10^{20}, 10^{22}]$ Pa · s
$E_{act}$	Activation energy	[150, 300] kJ/mol

Table 2: Parameters varied among different simulations

### 3 Results and discussion

Parameter	Description	Values
$\Delta t$	Timestep	$4 \cdot 10^6$ y
$T_{ref}$	Reference temperature	1600 K
$k_m$	Thermal conductivity	$4 \frac{W}{mK}$
$\kappa_m$	Thermal diffusivity	$1 \cdot 10^{-6} \frac{m^2}{s}$
$C_{p,MO}$	Heat capacity of the BMO	$1000 \frac{J}{kgK}$
$C_{p,m}$	Heat capacity of the mantle	$1200 \frac{J}{kgK}$
$L_{crist}$	Latent heat of crystallization	$4 \cdot 10^5 \frac{J}{kg}$

Table 3: Parameters held constant during all simulations

$T_{up}$  [between 1600 and 1900 K, Plesa et al., 2015] and examine the influence of the crustal  $\Lambda_{cr}$  and mantle  $\Lambda_m$  enrichment factors, in the ranges of [9, 15] and [0.1, 0.7], respectively. Finally, the reference viscosity  $\eta_{ref}$  is varied between  $10^{20}$  and  $10^{22}$  Pa · s, and the activation energies  $E_{act}$  between 150 and 300 kJ/mol. Other parameters held constant in all simulations are listed in Table 3.

### 3.3 Global input parameter variations

In the first set of simulations we vary each of the eight input parameters across the range of values listed in the Table 4 in all possible combinations, producing 11664 Mars interior evolution models in total. The variation of the magma ocean–mantle transition  $r_{MO}$  and its time dependency for all 11664 models is shown in Fig. 6.

As described in Sec.1, MO–mantle interface should lay, after 4500 Myr of evolution, at  $\sim 1800$  km radius in order to reconcile both geochemical and geodetical inferences on the size of the core. Thus, we consider as viable only models with a current MO-mantle transition in the range of [1700, 1850] km. To reduce the computation time, we dismiss models reaching a MO-mantle transition of  $r_{MO} < 1700$  km, as apparent in the Fig. 6.

With these constraints applied, we obtain 225 successful models, for which we keep track of the time evolution of the following parameters: location of the magma ocean-mantle transition  $r_{MO}$ , of the magma ocean thickness  $d_{MO}$ , of the bottom boundary layer thickness  $d_{bbl}$ , of the stagnant lid thickness  $d_{lid}$ , of the upper mantle temperature  $T_{up}$ , of the magma ocean temperature  $T_{MO}$ , and of the heat fluxes entering ( $q_{low}$ ) and leaving ( $q_{up}$ ) the mantle. These quantities for the 225 models are plotted in Fig. 7.

The data in Table 4 shows the amount of successful models for each value of the input parameter. A

### 3 Results and discussion

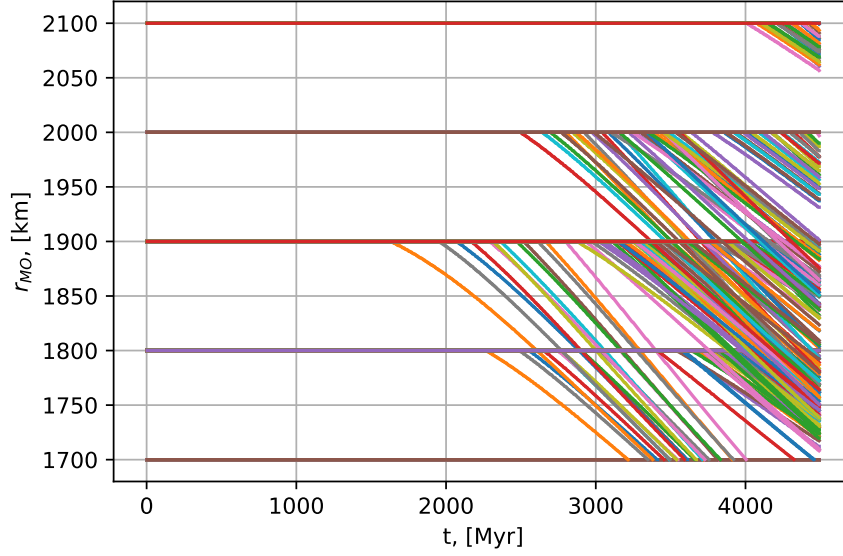


Figure 6: MO-mantle transition results across all of 11664 initial models. The models of interest are the ones with  $r_{MO}$  in range of [1700, 1850] km at 4500 Myr.

simple frequency analysis shows that most successful models have a core radius of 1400 km, a thin initial magma ocean (400 km), high initial magma ocean temperature (2100 K), average crustal (12) and mantle (0.5) enrichment, as well as low reference viscosity ( $10^{20}$  Pa s) and high activation energy ( $3 \cdot 10^5$  J/mol).

Most of the successful simulations require small core radius (1400 km) and a present-day thickness

$r_c$ , [km]	N	$d_{MO}$ , [km]	N	$T_{MO}$ , [K]	N	$T_{up}$ , [K]	N
1300	49	400	<b>137</b>	1900	0	1600	62
1400	<b>160</b>	500	65	2000	90	1700	59
1500	16	600	23	2100	<b>135</b>	1800	55
						1900	49
$\Lambda_{cr}$	N	$\Lambda_m$	N	$\eta_{ref}$ , [Pa · s]	N	$E_{act}$ , [J/mol]	N
9	33	0.1	6	$1 \cdot 10^{20}$	<b>172</b>	$1,50 \cdot 10^5$	61
12	<b>125</b>	0.3	76	$1 \cdot 10^{21}$	50	$2,25 \cdot 10^5$	70
15	67	0.5	<b>143</b>	$1 \cdot 10^{22}$	3	$3,00 \cdot 10^5$	<b>94</b>
		0.7	0				

Table 4: Amount of successful models  $N$  for the given input parameter value.

### 3 Results and discussion

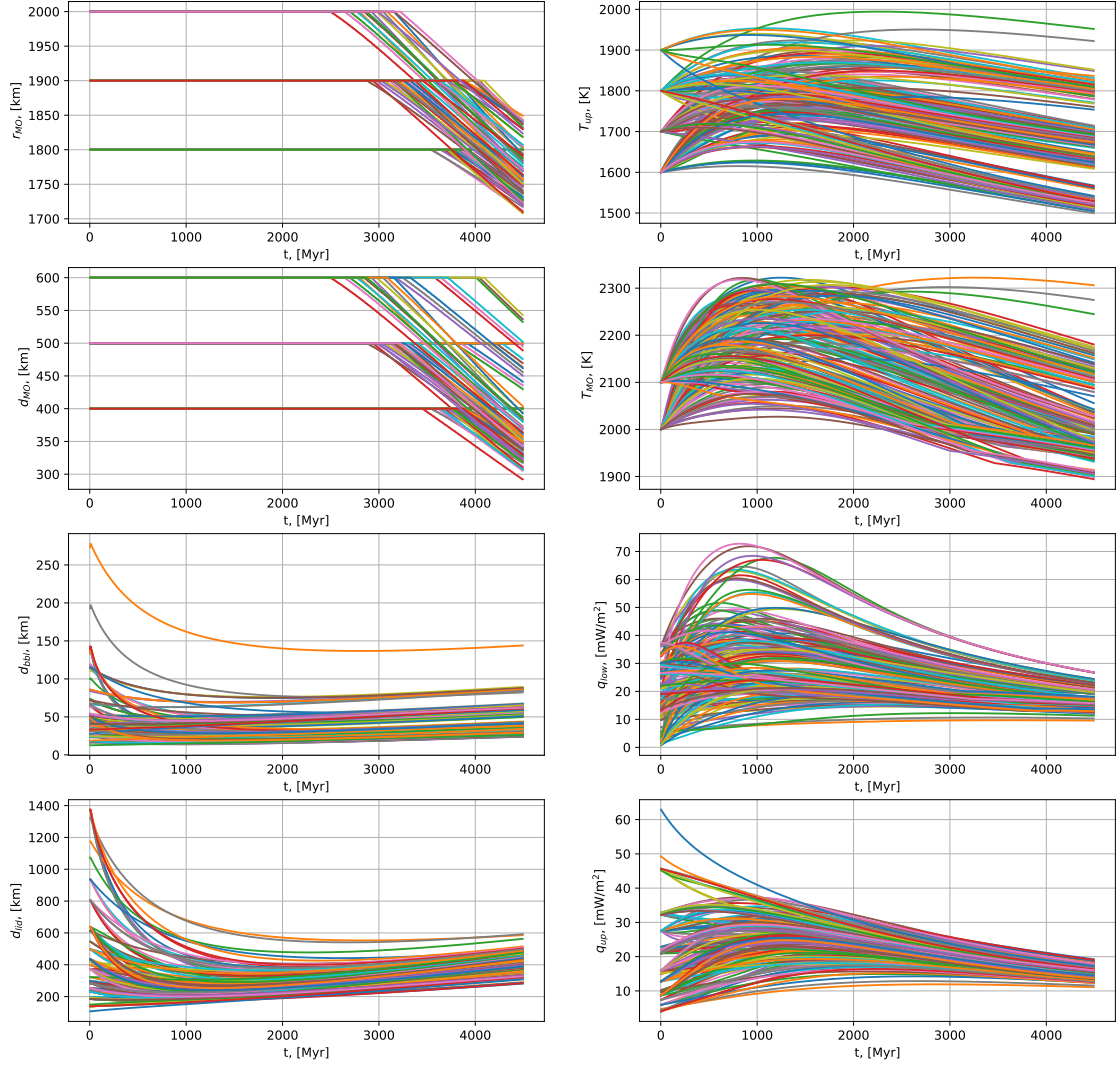


Figure 7: Parameter variations within the 225 considered plausible models.

of the magma ocean of [350, 400] km (Fig. 7), comparable both with the geochemical inference (small chemical core) of Rivoldini et al. [2011] and the geodetical inference (large liquid-to-solid transition) of Plesa et al. [2018]. The present day stagnant lid thickness  $d_{lid}$  for most of the successful models lay in the range of [300, 500] km, which is at least 100 km thicker than the recent estimates of Thiriet et al. [2019]. This discrepancy can be explained by the different modelling of the heat transport in the interior: while our model has a stagnant lid at the top of the mantle, the model used in the simulations by Thiriet et al. [2019] includes an upper boundary layer at the convective mantle - stagnant lid transition. If this upper boundary layer had a thickness similar to the bottom boundary layer, our results for  $d_{lid} - d_{bbl}$  would match the estimates of Thiriet et al.

[2019].

The time development of the upper mantle temperature  $T_{up}$  shows similarities with the mean mantle temperature development of Thiriet et al. [2019] with a main trend for a present-day value of  $\sim 1650 - 1750$  K while also showing two popular tendencies for  $\sim 1550$  K and  $\sim 1800$  K (Fig. 7). The value depends strongly on the initial input parameter values of the reference viscosity  $\eta_{ref}$  and the activation energy  $E_{act}$  (see Appendix, Fig. 16-17).

The present-day value for the magma ocean temperature  $T_{MO}$  lies in range [1950; 2150 K], which is comparable to the core-mantle boundary temperature  $T_{CMB}$  for the hot mantle models discussed by Rivoldini et al. [2011]. For most models, the value of  $T_{MO}$  is comparable with the results of the simulations for  $T_{CMB}$  of Plesa et al. [2015].

For most simulations the lower heat flux experiences a rapid increase within the first Gyr, associated with the extreme heat generation through the decay of the HPE. The present-day values for both fluxes are almost independent of the input parameters, a manifestation of the thermostat effect [e.g., Plesa et al., 2015]. The thermostat effect regulates the interior to such a degree, that the initial conditions have little or no influence on the present-day thermal state of Mars.

The clear trend of  $q_{up} \approx 15 \text{ mW/m}^2$  is slightly lower than the estimation of Thiriet et al. [2019] and Plesa et al. [2015]. This occurs due to the simpler approach taken in our models (no boundary layer between stagnant lid and convective mantle), which induces a more efficient heat removal and thus, more rapid reduction of surface heat flux in our simulations.

#### 3.4 Influence of input parameter variations on one model

Based on the trends of the 225 models listed in Table 4, we define here a reference model, characterised by the following set of parameters:  $r_c = 1400$  km,  $d_{MO} = 400$  km,  $T_{MO} = 2100$  K,  $T_{up} = 1750$  K,  $\Lambda_{cr} = 12$ ,  $\Lambda_m = 0.5$ ,  $\eta_{ref} = 1 \cdot 10^{20}$  Pa · s,  $E_{act} = 3 \cdot 10^5$  J/mol. The time evolution of the reference model is illustrated in Fig. 8.

We investigate the impact of each of the input parameters on the evolution of this reference model. To achieve this, we modify the value of a given parameter, while keeping the remaining seven constant. The resulting evolutions are found in Fig. (10-17) of the Appendix.

We find that the variation of the magma ocean initial temperature ( $T_{MO}$ ) and upper mantle initial temperature ( $T_{up}$ ) show no effect on the development of the models after a time of one Gyr. Variations of the crust ( $\Lambda_{cr}$ ) and mantle ( $\Lambda_m$ ) enrichment strongly impact the temperature of the MO-mantle ( $T_{MO}$ ) and mantle-lid interfaces ( $T_{up}$ ), as well as both upper mantle ( $q_{up}$ ) and

### 3 Results and discussion

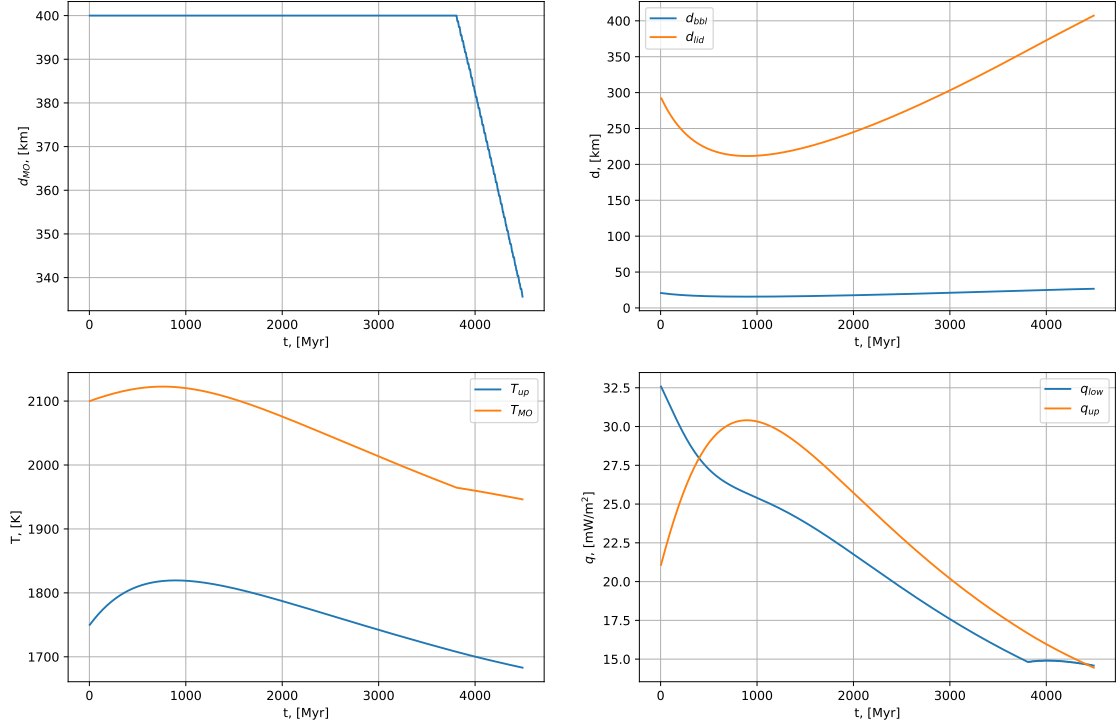


Figure 8: The development of the standard model with  $r_c = 1400$  km,  $d_{MO} = 400$  km,  $T_{MO} = 2100$  K,  $T_{up} = 1750$  K,  $\Lambda_{cr} = 12$ ,  $\Lambda_m = 0.5$ ,  $\eta_{ref} = 1 \cdot 10^{20}$  Pa  $\cdot$  s,  $E_{act} = 3 \cdot 10^5$  J/mol.

lower mantle ( $q_{low}$ ) heat fluxes. The reference viscosity ( $\eta_{ref}$ ) effects mostly the both interface temperatures ( $T_{up}$ ) and ( $T_{MO}$ ) and thus, the thickness of the magma ocean ( $d_{MO}$ ). An activation energy ( $E_{act}$ ) affects strongly the mantle-lid transition temperature ( $T_{up}$ ).

**Core radius  $r_c$ .** (Fig. 10) Smaller core radius  $r_c$  induces the smaller radius of the MO-mantle transition  $r_{MO}$  for a fixed MO thickness. The smaller core size also induces an earlier start of the magma ocean solidification due to the higher temperature of the liquidus at the bottom of the magma ocean (see Fig. 5).

**MO thickness  $d_{MO}$ .** (Fig. 11) Since a narrower magma ocean would have higher enrichment, the temperature shift of the liquidus would be bigger (Sec. 2.4), delaying the start of the MO solidification, which can be seen in Fig. 11. Magma ocean temperatures  $T_{MO}$  tend to differ during the most of the evolution, while reaching almost the same value for a modern day, in a clear contrast to the models with  $r_c$  variations.



### 3 Results and discussion

**Initial MO temperature  $T_{MO}$ .** (Fig. 12) The effect of different initial MO temperatures is absorbed within about the first 1.5 Gyr, a clear manifestation of the thermostat effect [Plesa et al., 2015].

**Initial upper mantle temperature  $T_{up}$ .** (Fig. 13) A higher  $T_{up}$  severely reduces the stagnant lid thickness  $d_{lid}$  and increases the upper mantle heat flux  $q_{up}$  for the first Gyr of the evolution. With higher  $T_{up}$  and temperature increase with depth, we also observe a  $T_{MO}$  increase. The development for the next three Gyr shows no prominent differences.

**Crust enrichment  $\Lambda_{cr}$ .** (Fig. 14) Models with  $\Lambda_{cr} > 13$  would require the enrichment of the magma ocean to be  $\Lambda_{cr} < 1$ , which would make it impossible for the magma ocean to be liquid at the beginning of the simulation. Only within the reference model with  $\Lambda_{cr} = 12$  the solidification of the magma ocean occurs. Lowering the crust enrichment implies higher magma ocean enrichment and thus, larger amount of heat generated within the MO. This results into a larger  $T_{MO}$  increase, followed in turn by the increase of the  $q_{low}$ ,  $T_{up}$  and  $q_{up}$ .

**Mantle enrichment  $\Lambda_m$ .** (Fig. 15) Extremely low mantle enrichment ( $\Lambda_m = 0.1$ ) models result into an extreme MO enrichment, leading to  $T_{MO}$  increase and, possibly, bottom of the mantle liquefaction. High mantle enrichment ( $\Lambda_m = 0.7$ ) would not cause the liquefaction of the magma ocean in first place.

**Reference viscosity  $\eta_{ref}$ .** (Fig. 16) Lowering the reference viscosity  $\eta_{ref}$  would significantly accelerate the heat transfer through the interior of the planet due to an increase of the Rayleigh number, and thus, an increase of the lower ( $q_{low}$ ) and upper ( $q_{up}$ ) mantle heat flux, leading to the earlier initiation of the magma ocean solidification.

**Activation energy  $E_{act}$ .** (Fig. 17) Since an activation energy  $E_{act}$  impacts the reference viscosity, and thus, the Rayleigh number (Eq. (20) and (18)), its impact is similar to the impact of the reference viscosity  $\eta_{ref}$ : in general higher upper mantle temperatures  $T_{up}$  and larger  $q_{low}$  in the early phases of the evolution.

### 3.5 Magmatic activity

The surface analysis of the planet indicates very recent volcanic activity on Mars [Hauber et al., 2011], meaning that rocks in the mantle are currently melting, thus producing magma in the interior that could possibly erupt at the surface. Magmatism occurs when the temperature in the mantle is locally above the mantle solidus temperature. The comparison of the temperature profile and the solidus profile as a function of time allows us to verify if our reference model is compatible with a current-day volcanically-active Mars. Fig. 9 illustrates that the reference model would produce magma in the mantle only for the first three Gyr.

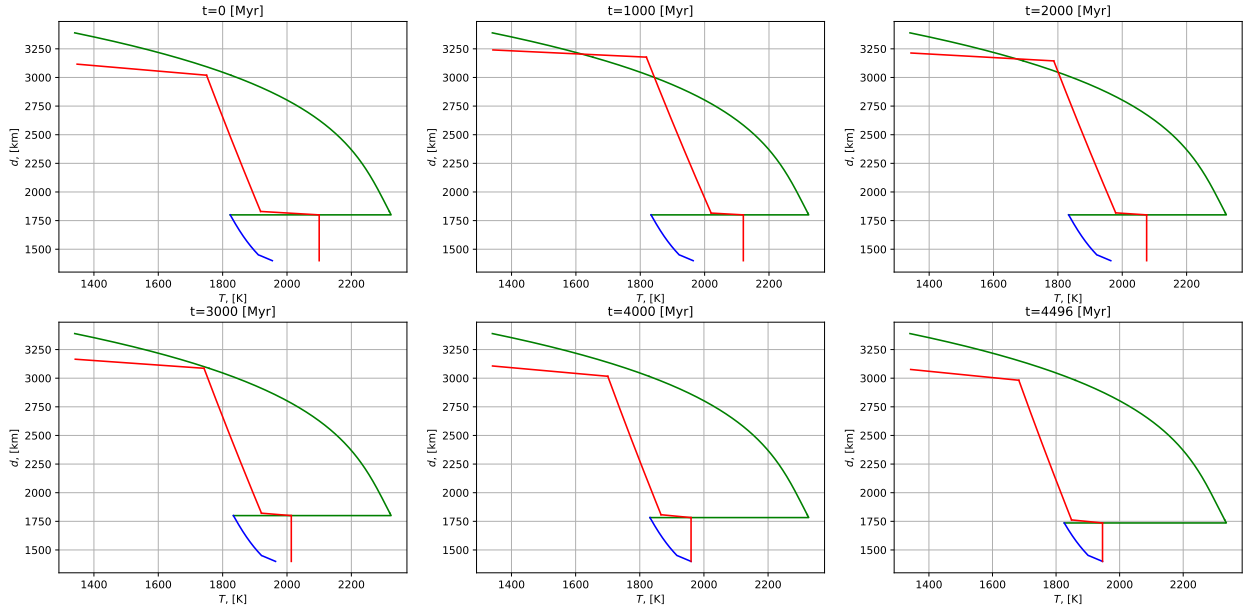


Figure 9: Solidus of the mantle (green), liquidus of the MO (blue) and the temperature profile (red) for the reference model during the interior evolution. The crossing of the red and green curves in the upper mantle indicates the possibility for the formation of the magma chamber.

## 4 Conclusions

Geochemical and geodetical estimates of the size of the core of Mars cover a large range of values (from  $\sim 1400$  km to  $\sim 1850$  km), yet they can be reconciled if a basal magma ocean with a thickness of  $\sim 400$  km is currently present on Mars. We performed simulations of the interior evolution of Mars with a basal magma ocean, which indicate that a present day magma ocean on Mars can exist, thus providing a possible way to reconcile the geochemical and geodetical estimates of the radius of the core of the planet [Rivoldini et al., 2011; Wang and Becker, 2017].

Based on the result of the successful simulations, a possible set of model parameters is:  $r_c = 1400$  km,  $d_{MO} = 400$  km,  $T_{MO} = 2100$  K,  $T_{up} = 1750$  K,  $\Lambda_{cr} = 12$ ,  $\Lambda_m = 0.5$ ,  $\eta_{ref} = 1 \cdot 10^{20}$  Pa·s,  $E_{act} = 3 \cdot 10^5$  J/mol. While this set of parameters seems to provide a viable explanation for the core-radius discrepancy, it fails at reproducing the observed long-lived volcanic activity of the planet and the expected surface heat flux. Considering the simplified approach used in the parameterized model and the promising results of the simulations, improving the model by using the approach of Thiriet et al. [2018] may further support our hypothesis that a basal magma ocean is currently present on Mars.

## 5 References

- Breuer, D. (2009). Dynamics and thermal evolution. volume 4: Astronomy, Astrophysics, and Cosmology of *Group VI: Astronomy and Astrophysics*, pages 254–270. Springer.
- Elkins-Tanton, L. T. (2012). Magma Oceans in the Inner Solar System. *Annual Review of Earth and Planetary Sciences*, 40(1):113–139.
- Goossens, S., Sabaka, T. J., Genova, A., Mazarico, E., Nicholas, J. B., and Neumann, G. A. (2017). Evidence for a low bulk crustal density for Mars from gravity and topography. *Geophysical Research Letters*, 44(15):7686–7694.
- Grott, M. and Breuer, D. (2008). The evolution of the martian elastic lithosphere and implications for crustal and mantle rheology. *Icarus*, 193(2):503–515.
- Hauber, E., Brož, P., Jagert, F., Jodłowski, P., and Platz, T. (2011). Very recent and wide-spread basaltic volcanism on Mars. *Geophysical Research Letters*, 38(10).
- NASA (2018 (accessed August 12, 2020)). Mars fact sheet. <https://nssdc.gsfc.nasa.gov/planetary/factsheet/marsfact.html>.
- Neumann, G. A., Zuber, M. T., Wieczorek, M. A., McGovern, P. J., Lemoine, F. G., and Smith, D. E. (2004). Crustal structure of Mars from gravity and topography. *Journal of Geophysical Research: Planets*, 109(E8).
- Plesa, A.-C., Grott, M., Tosi, N., Breuer, D., Spohn, T., and Wieczorek, M. A. (2016). How large are present-day heat flux variations across the surface of Mars? *Journal of Geophysical Research: Planets*, 121(12):2386–2403.
- Plesa, A.-C., Padovan, S., Tosi, N., Breuer, D., Grott, M., Wieczorek, M. A., Spohn, T., Smrekar, S. E., and Banerdt, W. B. (2018). The Thermal State and Interior Structure of Mars. *Geophysical Research Letters*, 45(22):12,198–12,209.
- Plesa, A.-C., Tosi, N., and Breuer, D. (2014). Can a fractionally crystallized magma ocean explain the thermo-chemical evolution of Mars? *Earth and Planetary Science Letters*, 403:225 – 235.
- Plesa, A.-C., Tosi, N., Grott, M., and Breuer, D. (2015). Thermal evolution and Urey ratio of Mars. *Journal of Geophysical Research: Planets*, 120(5):995–1010.
- Reese, C. C., Solomatov, V. S., and Moresi, L. N. (1998). Heat transport efficiency for stagnant lid convection with dislocation viscosity: Application to Mars and Venus. *J. Geophys. Res.*, 103(E6):13643–13658.

## 5 References

- Rivoldini, A., Hoolst, T. V., Verhoeven, O., Mocquet, A., and Dehant, V. (2011). Geodesy constraints on the interior structure and composition of Mars. *Icarus*, 213(2):451–472.
- Ruedas, T. and Breuer, D. (2017). On the relative importance of thermal and chemical buoyancy in regular and impact-induced melting in a Mars-like planet. *J. Geophys. Res.*, 122:1554–1579.
- Stevenson, D. J., Spohn, T., and Schubert, G. (1983). Magnetism and thermal evolution of the terrestrial planets. *Icarus*, 54(3):466 – 489.
- Thiriet, M., Breuer, D., Michaut, C., and Plesa, A.-C. (2019). Scaling laws of convection for cooling planets in a stagnant lid regime. *Physics of the Earth and Planetary Interiors*, 286:138–153.
- Thiriet, M., Michaut, C., Breuer, D., and Plesa, A.-C. (2018). Hemispheric Dichotomy in Lithosphere Thickness on Mars Caused by Differences in Crustal Structure and Composition. *Journal of Geophysical Research: Planets*, 123(4):823–848.
- Turcotte, D. and Schubert, G. (2014). *Geodynamics*. Cambridge University Press, 3 edition.
- Wang, Z. and Becker, H. (2017). Chalcophile elements in Martian meteorites indicate low sulfur content in the Martian interior and a volatile element-depleted late veneer. *Earth and Planetary Science Letters*, 463:56 – 68.
- Williams, J.-P. and Nimmo, F. (2004). Thermal evolution of the Martian core: Implications for an early dynamo. *Geology*, 32(2):97–100.
- Wänke, H. and Dreibus, G. (1994). Chemistry and accretion history of Mars. *Philosophical Transactions of the Royal Society of London. Series A: Physical and Engineering Sciences*, 349(1690):285–293.
- Yoder, C. F., Konopliv, A. S., Yuan, D. N., Standish, E. M., and Folkner, W. M. (2003). Fluid core size of Mars from detection of the solar tide. *Science*, 300:299–303.

**6 Appendix**

Isotope	$H_0$ , [W kg <sup>-1</sup> ]	$A$	$\tau$ ,[a]	$C$ ,[ppb]
<sup>40</sup> K	$2.92 \cdot 10^{-5}$	$1.19 \cdot 10^{-4}$	$1.25 \cdot 10^9$	$305 \cdot 10^3$
<sup>232</sup> Th	$2.64 \cdot 10^{-5}$	1	$1.40 \cdot 10^{10}$	56
<sup>235</sup> U	$5.69 \cdot 10^{-4}$	0.0071	$7.04 \cdot 10^8$	16
<sup>238</sup> U	$9.46 \cdot 10^{-5}$	0.9928	$4.47 \cdot 10^9$	16

Table 5: Specific heat production rate  $H_0$ , abundance  $A$ , half life  $\tau$  and concentration  $C$  obtained from Breuer [2009] and Wänke and Dreibus [1994].

## 6 Appendix

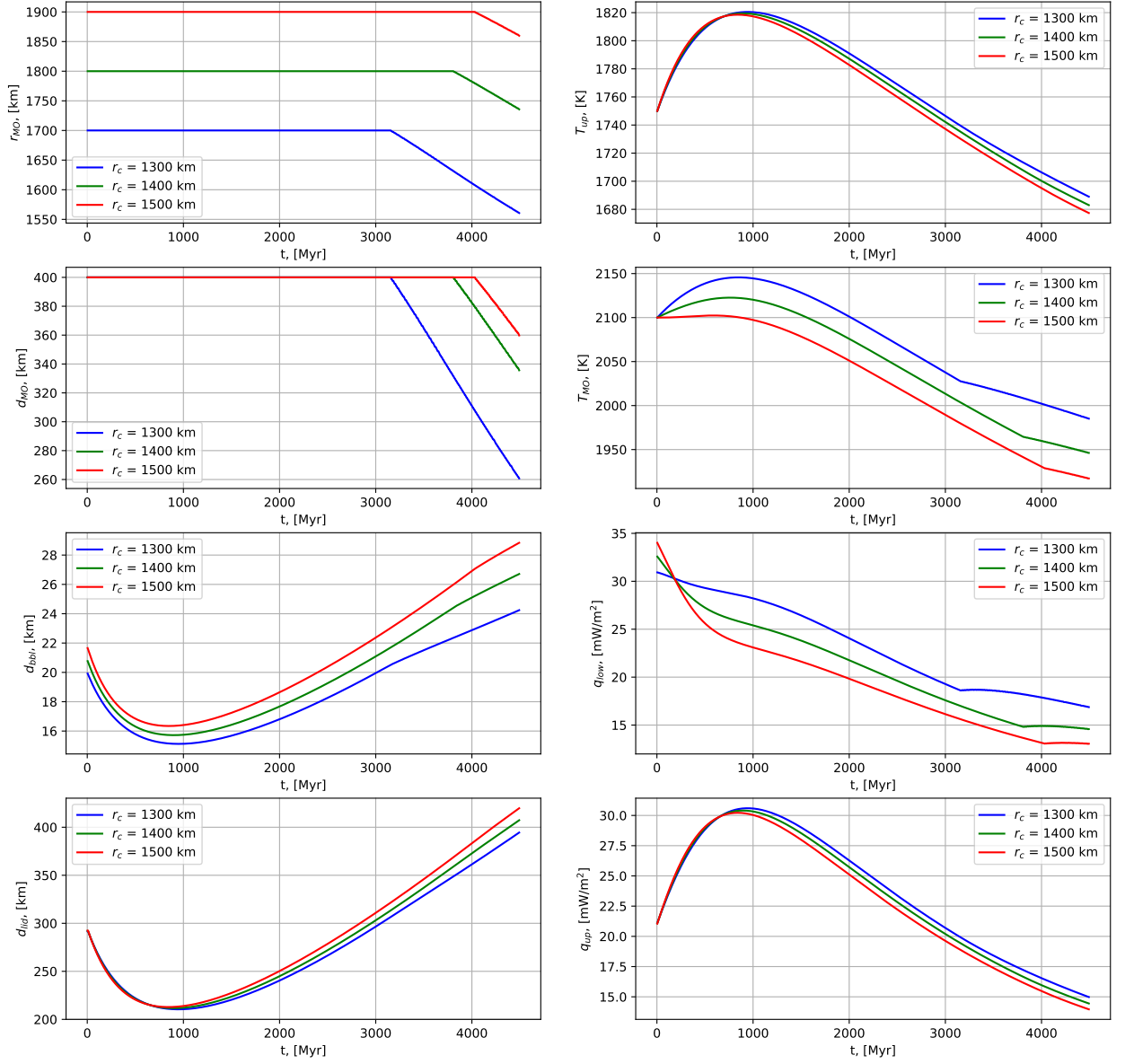


Figure 10: Impact of the core radius  $r_c$  onto the generic model.

## 6 Appendix

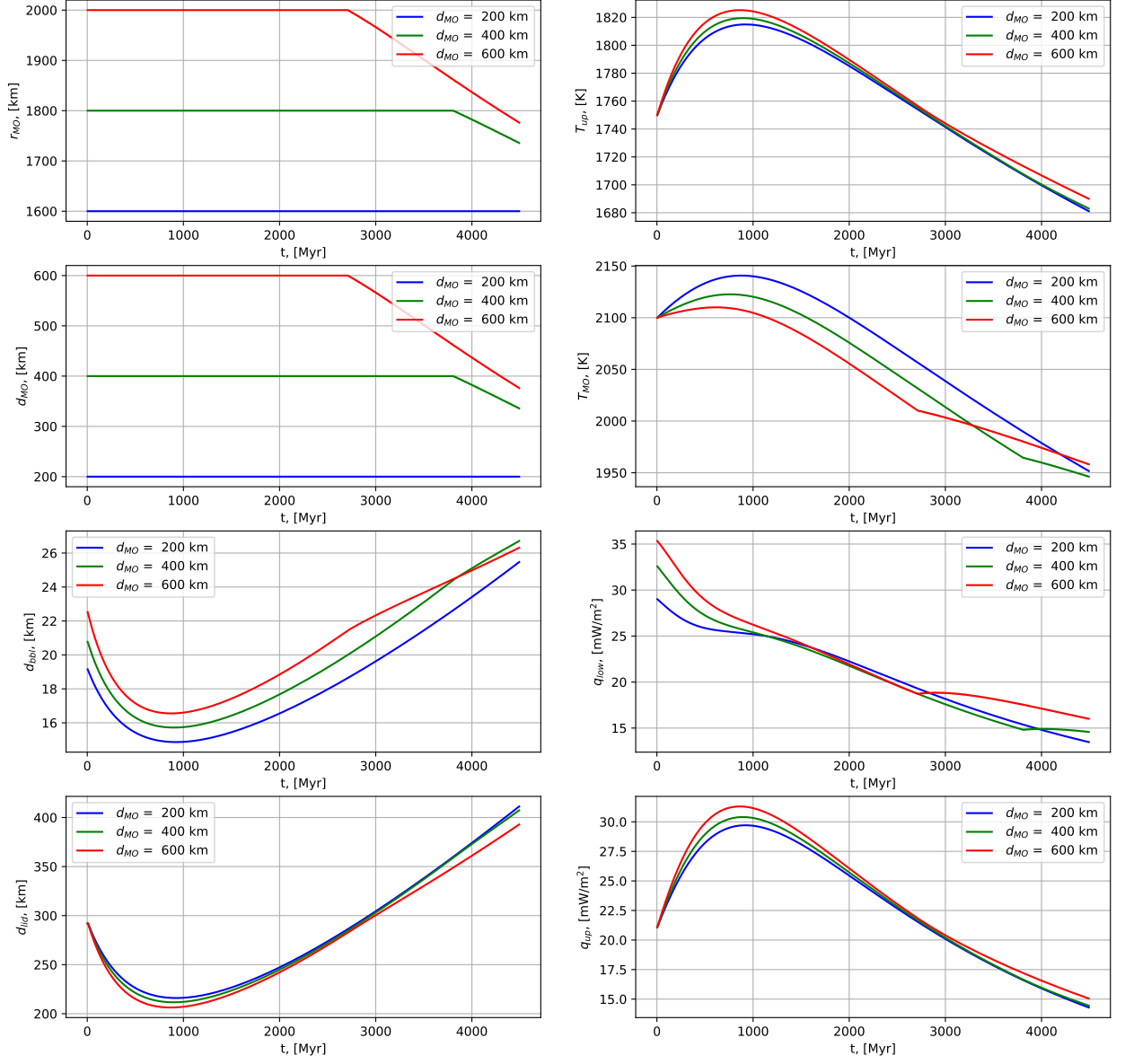


Figure 11: Impact of the magma ocean thickness  $d_{MO}$  onto the generic model.



## 6 Appendix

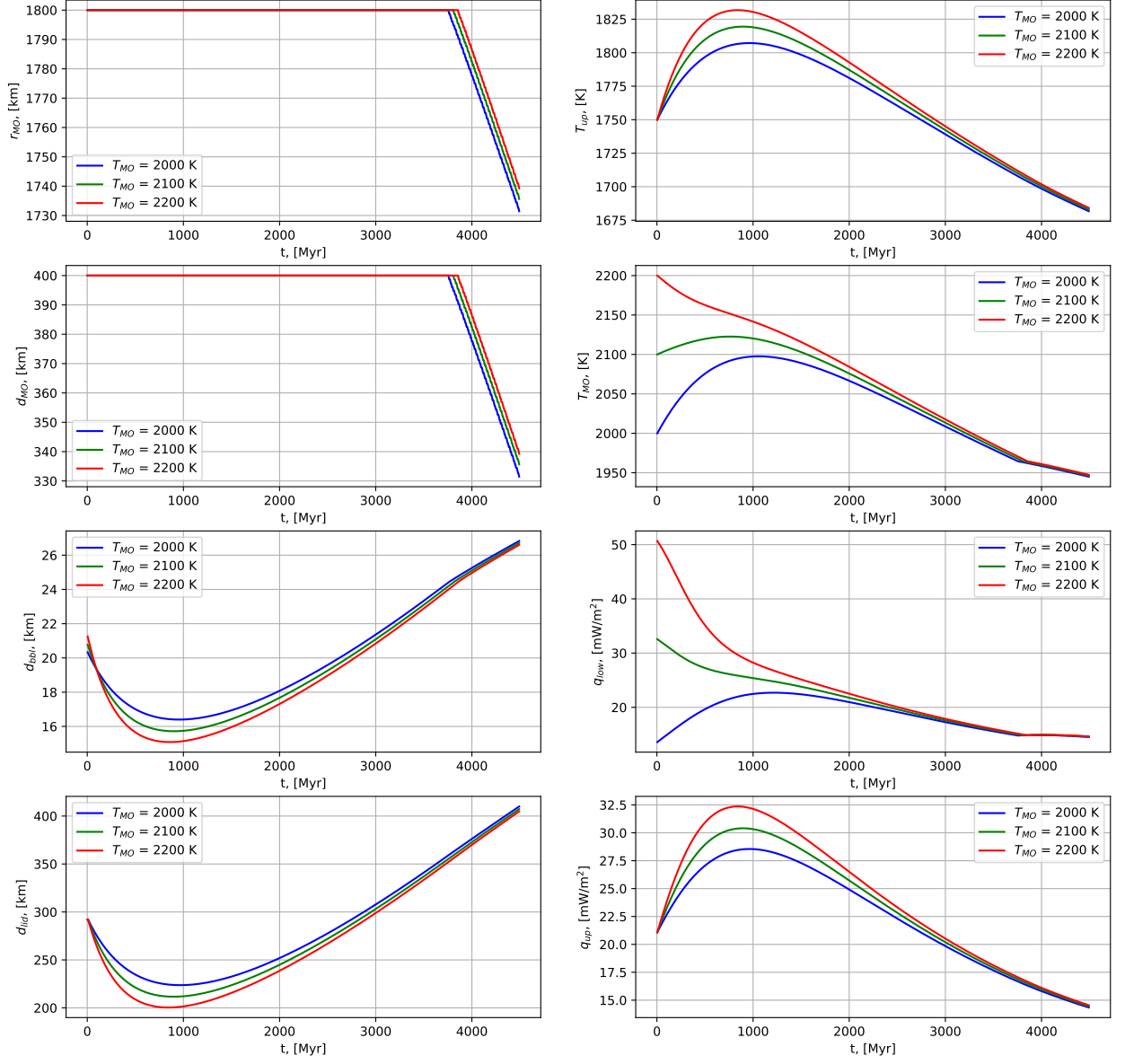


Figure 12: Impact of the magma ocean initial temperature  $T_{MO}$  onto the generic model.

## 6 Appendix

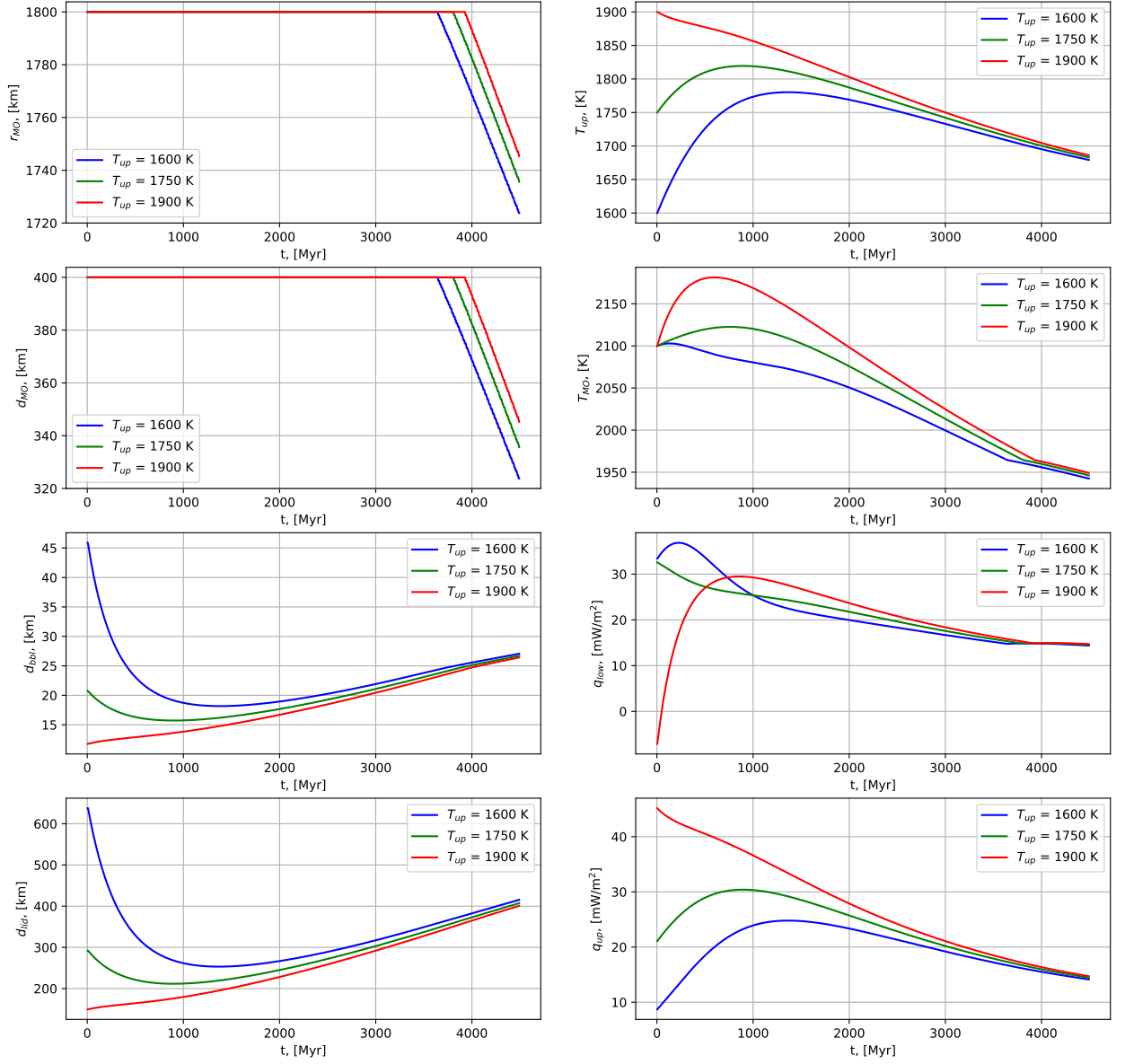


Figure 13: Impact of the upper mantle temperature  $T_{up}$  onto the generic model.

## 6 Appendix

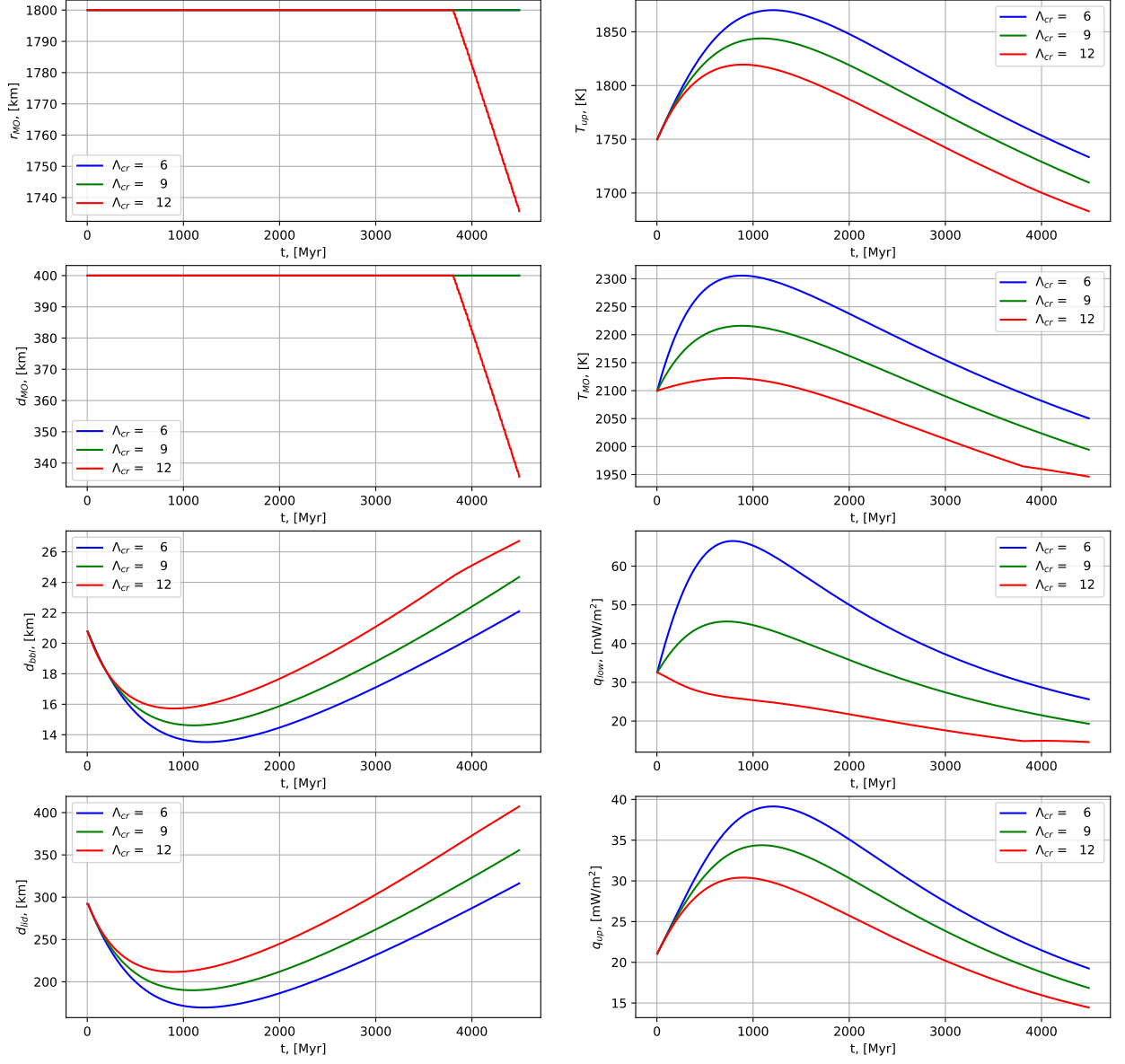


Figure 14: Impact of the crust enrichment factor  $\Lambda_{cr}$  onto the generic model.

## 6 Appendix

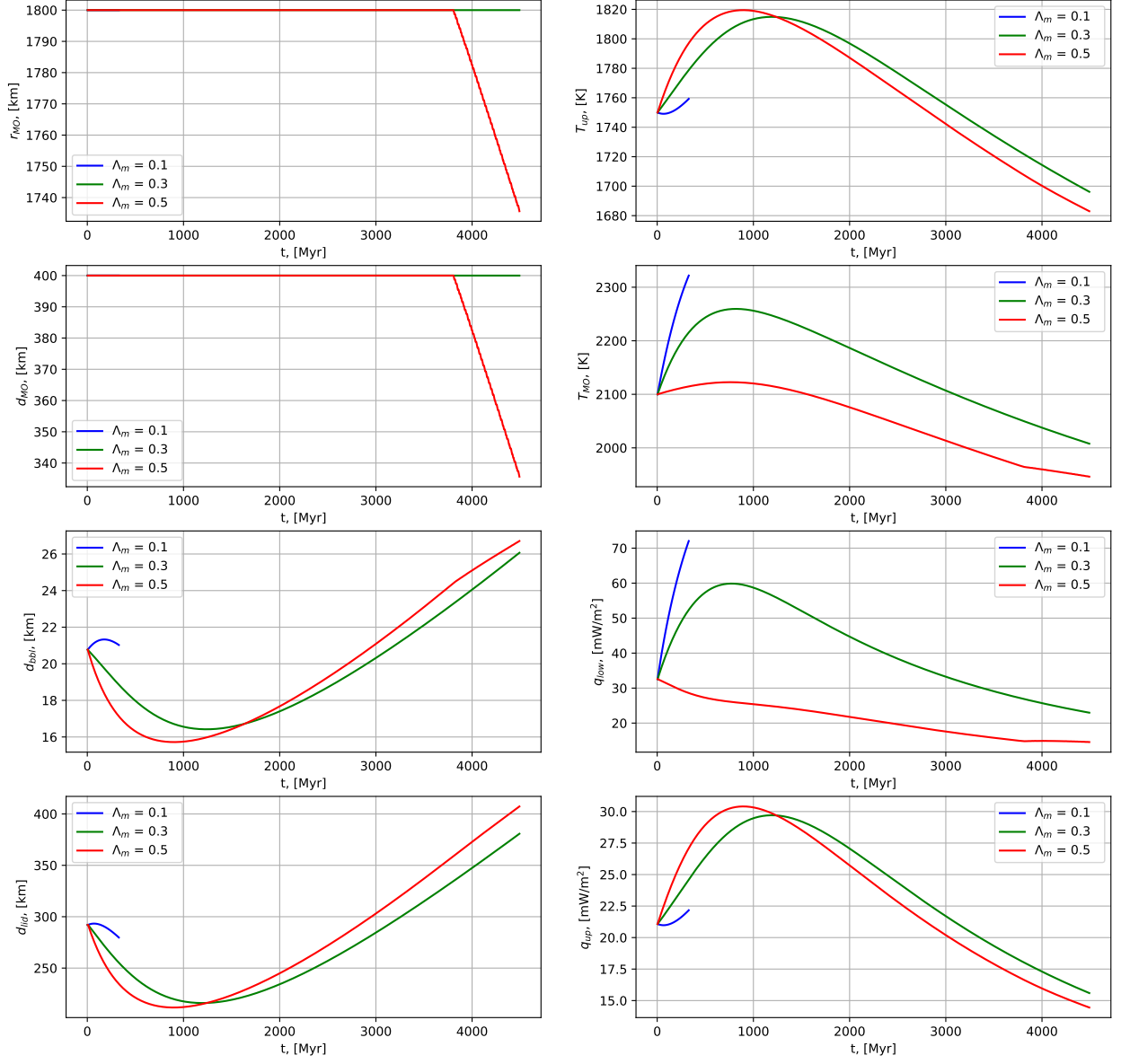


Figure 15: Impact of the mantle enrichment factor  $\Lambda_m$  onto the generic model.

## 6 Appendix

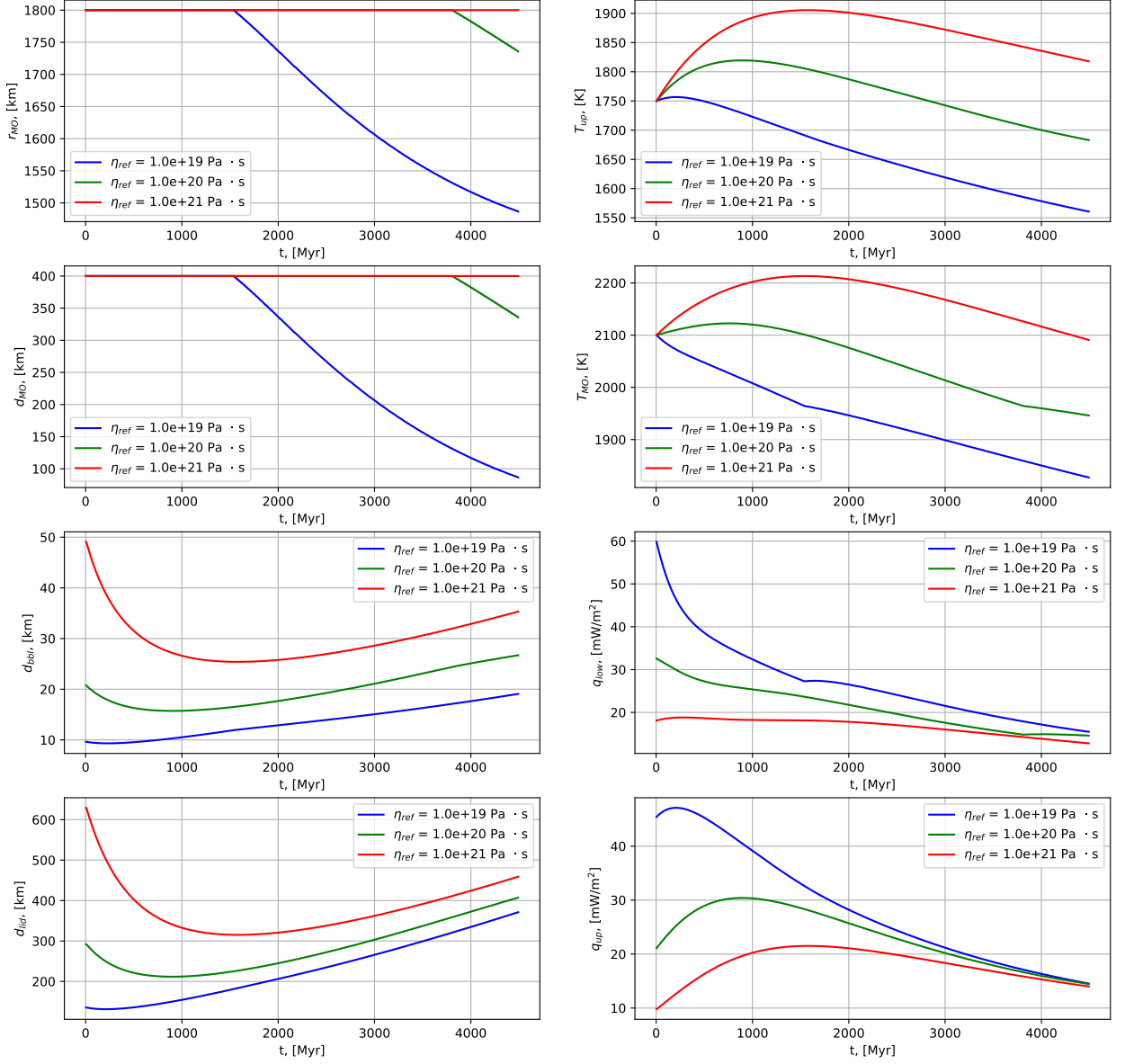


Figure 16: Impact of the reference viscosity  $\eta_{ref}$  onto the generic model.

## 6 Appendix

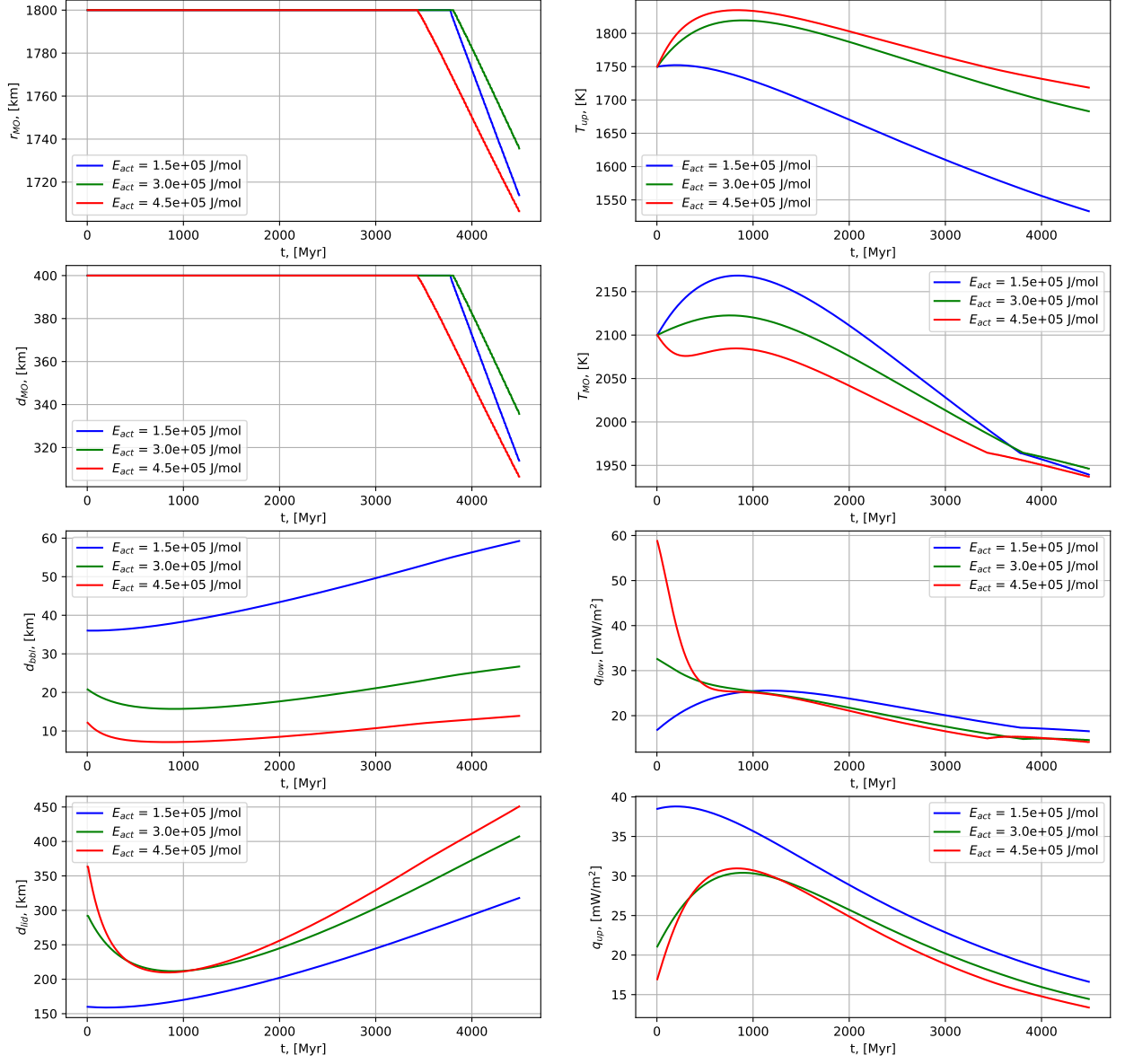


Figure 17: Impact of the activation energy  $E_{act}$  onto the generic model.